(NASA-CR-175745) A STUDY OF THE GENERATION MECHANISMS OF HIGH LATITUDE AND EQUATORIAL F-REGION IRREGULARITIES USING DE-2 DATA Semiannual Report, 1 Aug. 1984 - 31 Jan. 1985 (Emmanuel Coll.) 26 p HC A03/MF A01 G3/46

N85-27423

Unclas 21182

1. TITLE: A STUDY OF THE GENERATION MECHANISMS OF HIGH-LATITUDE AND EQUATORIAL F-REGION IRREGULARITIES USING DE-2 DATA

2. TYPE OF REPORT: SEMI-ANNUAL REPORT

3. PRINCIPAL INVESTIGATOR: DR. SUNANDA BASU

4. GRANTEE INSTITUTION: EMMANUEL COLLEGE
PHYSICS RESEARCH DIVISION
400 THE FENWAY
BOSTON MA 02115

5. GRANT NUMBER: NAG 5-456

6. PERIOD OF REPORT: AUGUST 1, 1984 - JANUARY 31, 1985

INTRODUCTION

The DE-2 spacecraft is an excellent tool for studying high-latitude irregularities as many different instruments are on board to measure various energy inputs into the magnetosphere-ionosphere system. Table I lists the instruments and the quantities they measure together with the names of the Principal Investigators (Hoffman et al., 1981). Of the instruments listed, the RPA, IDM, LAPI, MAGB, and VEFI are particularly appropriate for the study of high latitude irregularities. In this report characteristics of small scale (~10 km and smaller) density irregularities in the various domains of the high latitude F-region in the winter (i.e., dark) hemisphere are examined. The DE-2 spacecraft has made it possible for the first time to study simultaneously on a systematic basis the spectral characteristics of not only the density irregularities but of the velocity irregularities, as well. Density irregularity spectra near auroral acceleration and shear regions have been studied by Basu et al. (1984) using AE-D data.

RESULTS

We begin our study of high latitude irregularity characteristics by choosing the DE-2 orbit #3223 observed on March 8, 1982. It had the additional advantage of passing very close to two ground stations from which scintillation measurements were being conducted. Figure 1 shows the Goose Bay and Thule intersection points and the noon-midnight crossing of the satellite orbit. The coordinate system used to plot the pass is geographic latitutde and solar local time. A MLT-invariant latitude grid is superimposed for reference. The three-dimensional vector velocity obtained by combining drift measurements from the IDM and RPA is plotted along the track. We find two regions of enhanced convection velocities: one in the auroral oval close to the Goose Bay intersection and the other in the polar cap poleward of the Thule intersection point. Figures 2a and b show enlarged pictures of the two regions of enhanced drifts together with field aligned current measurements obtained from MAGB. It may be observed that the large drift velocities occur at the interface of a downward and an upward current system.

The particle precipitation measured by LAPI is shown in Figures 3a and b. Figure 3a shows particle precipitation at two pitch angles 0° and 45° in the midnight auroral oval and polar cap whereas Figure 3b shows precipitation characteristics in the dayside cusp. We note that the precipitation

between 0338-0339 UT is highly structured (probably associated with discrete visual structures) with some of the peaks reaching total energies in excess of 10 ergs $(cm^2\ s)^{-1}$ (computed by using the method of Lin and Hoffman (1982)) while that between 0336-0338 UT is relatively unstructured and associated with diffuse aurora. The low energy precipitation associated with the cusp is observed between 0347-0348 UT.

In Figures 4a and b we show the ion concentration, the horizontal component of the ion drift measured by the IDM, and the field-aligned current in the auroral oval, polar cap and dayside cusp. It is important to note that the ion concentration is approximately $10^6\ cm^{-3}$ within the polar cap at the 400 km altitude of the satellite. Figure 5 shows the IDM horizontal component of the drift throughout the high latitude region, as well as, the irregularity amplitude $\Delta N/N$ measured by the RPA every 8 sec along the satellite track. Large discrete irregularity structures are seen in the dayside cusp and in the polar cap. Thus one expects large discrete scintillation structures as the irregularities drift across the satellite ray path from Thule. The irregularity characteristics are not as discrete in the auroral oval though and scintillations caused by such an environment are expected to be much more continuous in nature. The scintillations obtained from Thule and Goose Bay will be presented later.

Our major interest in the DE-2 study is in getting more information on the small scale density and velocity structure of the high latitude irregularities. We have noted from Figure 5 that the largest amplitude irregularity structure (between 0346-0347) is observed in the dayside cusp in conjunction with large velocity structure, field aligned current flow and soft particle precipitation. The large structure between 0344 and 0345 UT is obviously one that has been convected into the dayside polar cap by the antisunward drift that we observe from Figure 1. The convection argument is strengthened by the fact that no perceptible drift, field aligned current or precipitation structure is associated with the density structure. The structure in the density was most probably developed in the cusp and the long lifetimes of the moderately large scale ($\sim$10 km - 1 km) irregularities (Vickrey and Kelley, 1982) is in all likelihood responsible for the integrity of the structure. We shall show, however, that the spectrum of the drifted structure exhibits an erosion of the smaller scales. The density structure at 0341, in the nightside cap seems to be convected also and in this case the irregularity amplitude is smaller than the convected structure in the dayside cap probably as a consequence of being in the convection regime for a longer period of time. The Thule scintillation observations are most probably related to this density structure.

From Figures 3a, 4a, and 5 we note that the nightside auroral oval is another source region for irregularities with very structured precipitation taking place and being accompanied by structured horizontal drifts and field-aligned currents. There is another large irregularity structure associated with the diffuse aurora and the so-called boundary blob (Tsunoda and Vickrey, 1984) between 0336-0337 UT.

In Figures 6a, b and c we show respectively the electron density and horizontal cross track and vertical velocity spectra in the 3 domains we have discussed earlier, namely, the cusp, the dayside polar cap and the nightside auroral oval. In the cusp at 034639 UT the irregularity amplitude is found to be 17.8%. The spectrum for the density measurements has a slope of -1.9 between 1 km and 200 m and the horizontal velocity has a slope of -1.8 between 1 km and 400 m. It should be noted that the vertical velocity spectra does not have any significant power spectral densities at these scalelengths. The solid line joining points which are 125 m and shorter in scalelength come from the Wideband filter outputs and considerable power is seen even at these short scalelengths.

In contrast, the drifted irregularity structure seen in the dayside polar cap, in spite of its large irregularity amplitude of 21.5% (dominated by scales $\sim$ 10 km) has little power at the short scales covered by the Wideband filter

output range. The slope of the density spectra is steeper being -2.7 and the horizontal velocity spectrum is basically noiselike since it has insignificant power at the short scales. If one compares the power at different scalelengths, it is apparent that the primary erosion has taken place at scalelengths shorter than 200 m. The a.c. electric field data will shed some more light on the cusp density and velocity structure and those associated with the convected structure in the polar cap.

In Figure 6c, the nighttime auroral oval density and velocity structure seen at 033823 UT again look similar to those observed in the cusp. The shorter scale irregularities, which were found to be absent in the convected polar cap structure, are again observed in the oval. Thus it is the shorter scales which are crucial in identifying locally generated structures.

Finally we study the a.c. electric field fluctuation spectrum provided by the VEFI instrument. Figures 7a and b show the 1-sec spectra in the cusp and in the convected irregularity spectra respectively. The cusp spectrum obtained at 034650 had a k^{-2} slope between 6 Hz and 96 Hz and a much steeper spectrum approximating k^{-5} between 384 and 768 Hz. There is a shoulder between the two spectral regimes between 200-300 Hz which may be due to a specific turbulence mechanism. The convected spectrum shown in Figure 7b, on the other hand, shows a single k^{-3}

spectrum. It is rather interesting to note that the a.c. electric field spectrum shows a definite spectral shape similar to the density spectrum shown in Figure 6b, while the horizontal velocity spectrum shows noiselike behavior. This could be due to the greater sensitivity of the VEFI instrument. In Figure 7c we show the noise threshold of the VEFI instrument. Comparing Figure 7b with 7c, we find that some excess power is seen up to ∿100 Hz (i.e., 80 m scalelength) in the convected structure. The a.c. electric field spectra corresponding to the auroral oval sample shown in Figure 7c has been requested from Goddard Space Flight Center and it is hoped that it will be available in the near future. This will enable us to study, in particular, the short-scale irregularity behavior in various regimes of the high latitude ionosphere.

Figures 8 and 9 show phase and amplitude scintillations observed at Goose Bay and Thule at the time of the DE-2 satellite pass. While discrete structures were observed at Thule, the Goose Bay scintillations were more continuous in nature as expected from the respective irregularity morphology shown in Figure 5. Further studies of both scintillation and in-situ irregularity structures will be made to determine the extent to which in-situ density structures are mapped in phase and intensity scintillation data.

REFERENCES

Basu, Su., S. Basu, E. MacKenzie, W.R. Coley, W.B. Hanson, and C.S. Lin, F-region electron density irregularity spectra near auroral acceleration and shear regions, J. Geophys. Res., 89, 5554, 1984.

Hoffman, R.A., G.D. Hogan, and R.C. Maehl, Dynamics Explorer spacecraft and ground operations system, Space Sci. Inst., 5, 349, 1981.

Lin, C.S. and R.A. Hoffman, Narrow bursts of intense electron precipitation fluxes within inverted-V events, Geophys. Res. Lett., 9, 211, 1982.

Tsunoda, R.T. and J.F. Vickrey, Evidence of east-west structure in large-scale F-region plasma enhancements in the auroral region, Submitted to J. Geophys. Res., 1984.

Vickrey, J.F. and M.C. Kelley, The effects of a conducting E-layer on classical F-region cross-field plasma diffusion, J. Geophys. Res., 87, 4461, 1982.

TABLE I

Instruments for the low altitude mission (DE-B)

Instrument	Acronym	Instrumentation	Measurement	Investigator
Magnetometer	MAG-B	Three axis fluxgate	Vector magnetic field	M. Sugiura
Vector electric field instrument	VEFI	Triaxial double probes	Vector electric field Variational electric field	N. Maynard
Neutral atmosphere composition spectrometer	NACS	Quadrapole mass spectrometer	Neutral composition and density	G. Carignan
Wind and temperature spectrometer	WATS	Retarding potential quadrupole mass spectrometer	Vertical, zonal and meridional components of neutral wind	N. Spencer
Fabry-Perot interferometer	FPI	Flat plate interferometer with zenith angle scan	Drift and temperature of neutral and ionic atomic oxygen	P. Hays
Ion drift meter	IDM	Collimated ion trap with segmented collectors	Components of ion drift normal to spacecraft velocity	R. Heelis
Retarding potential analyzer	RPA	Retarding potential analyzer	Thermal ion density, temperature, irregularities. Ram component of ion drift	W. Hanson
Langmuir probe	LANG	Cylindrical electrostatic probes	Electron temperature and density, ion density, irregularities	L. Brace
Low altitude plasma instrument	LAPI	15 electrostatic analyzers and two Geiger counters	Ion and electron distributions to 30 keV. High energy monitors	J. Winningham

DE-2 MAR. 8, 1982 ORBIT #3223

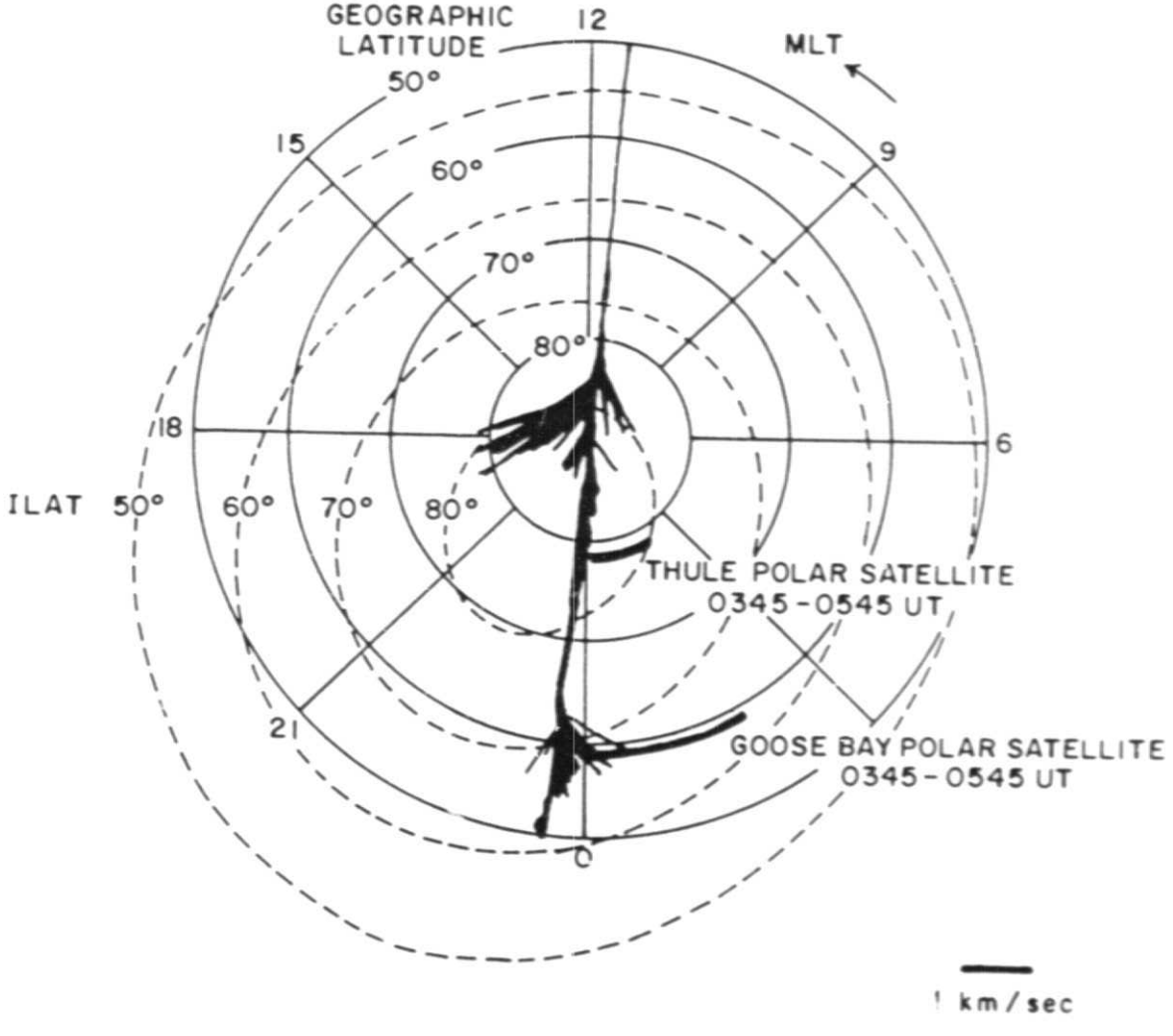

Figure 1

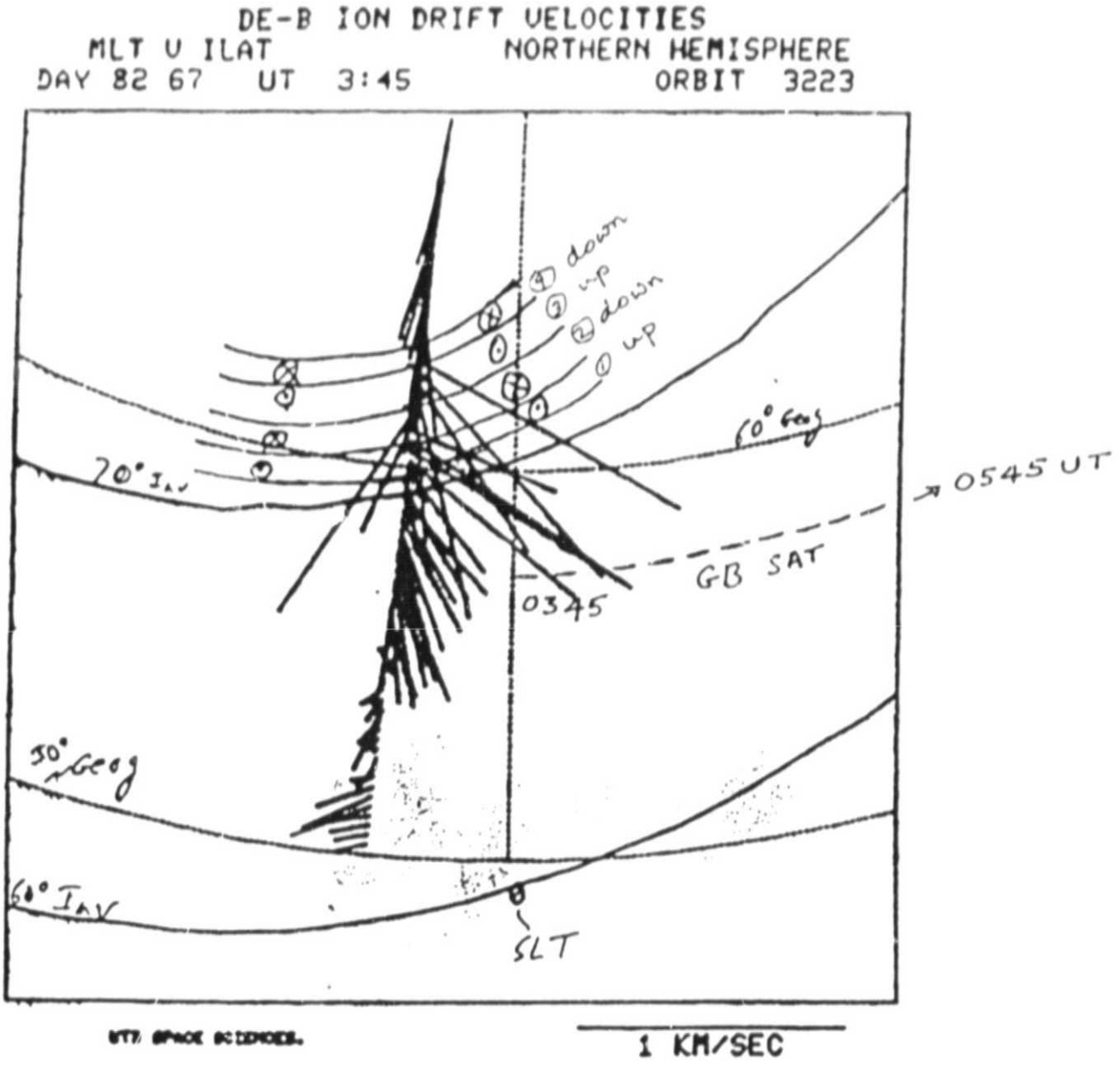

Evening sector vector ion drift velocities with locations of field-aligned current sheets superimposed and satellite intersection.

Figure 2a

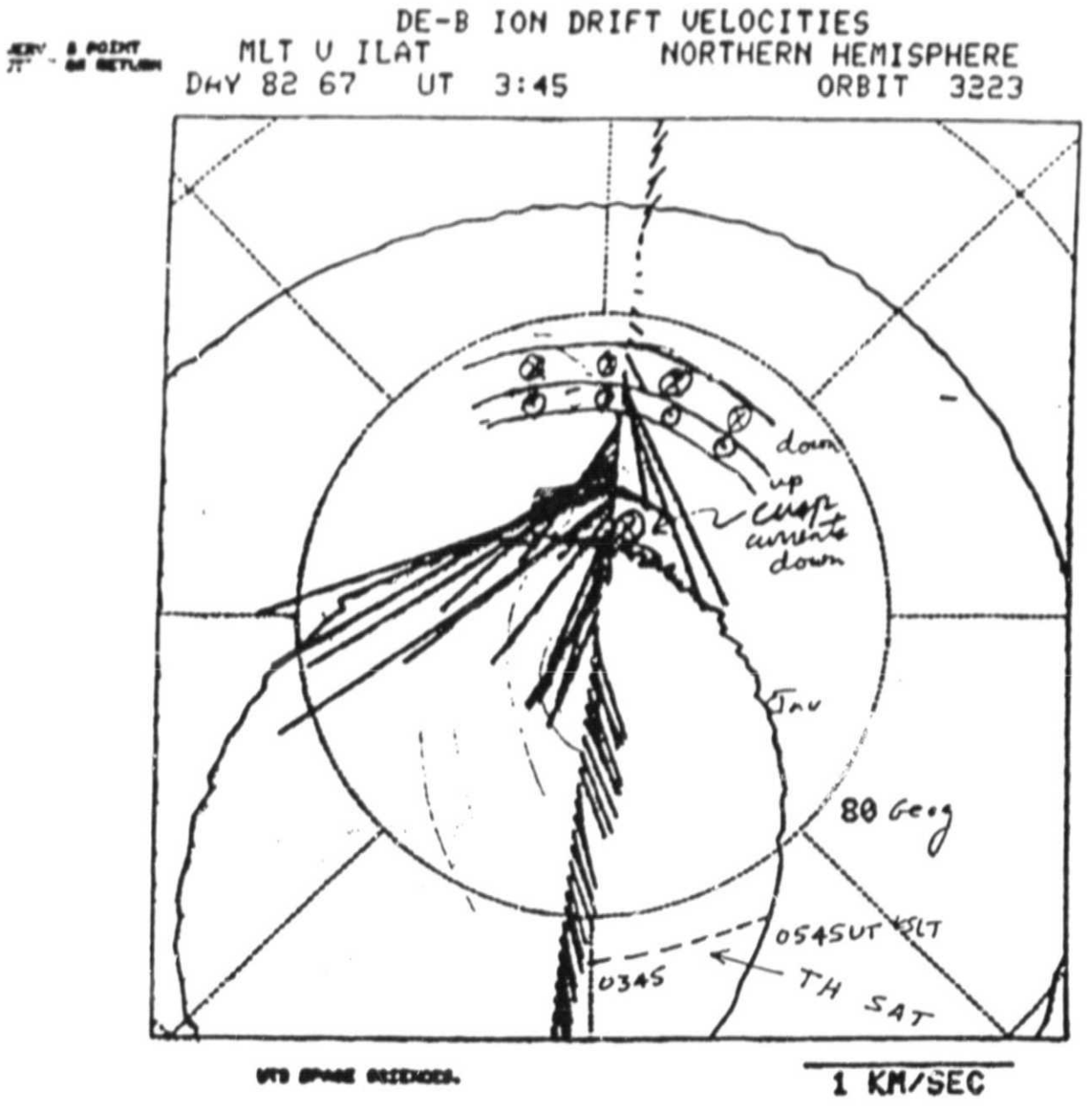

Polar cap vector ion drift velocities with locations of field-aligned current sheets superimposed and satellite intersection.

Figure 2b

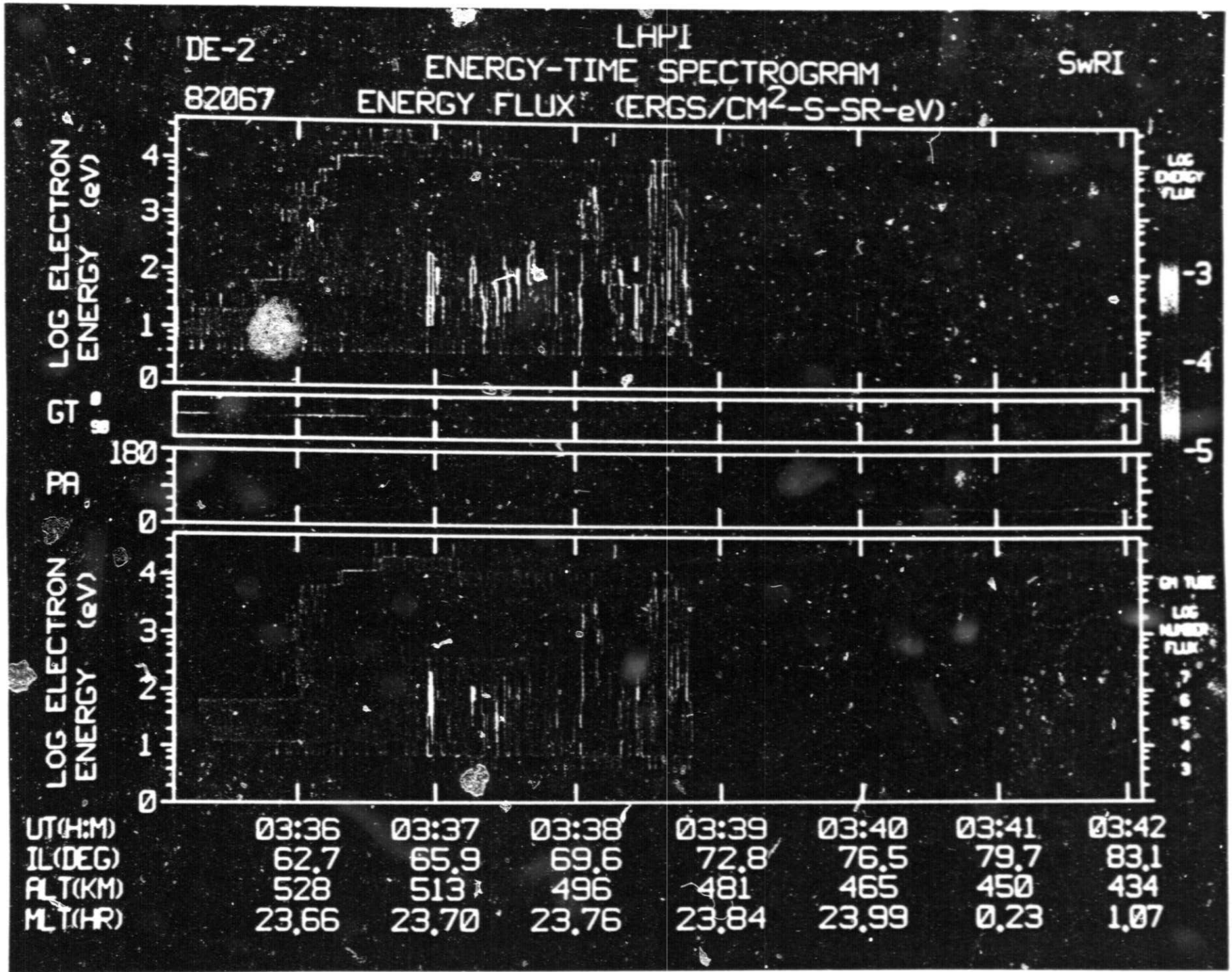

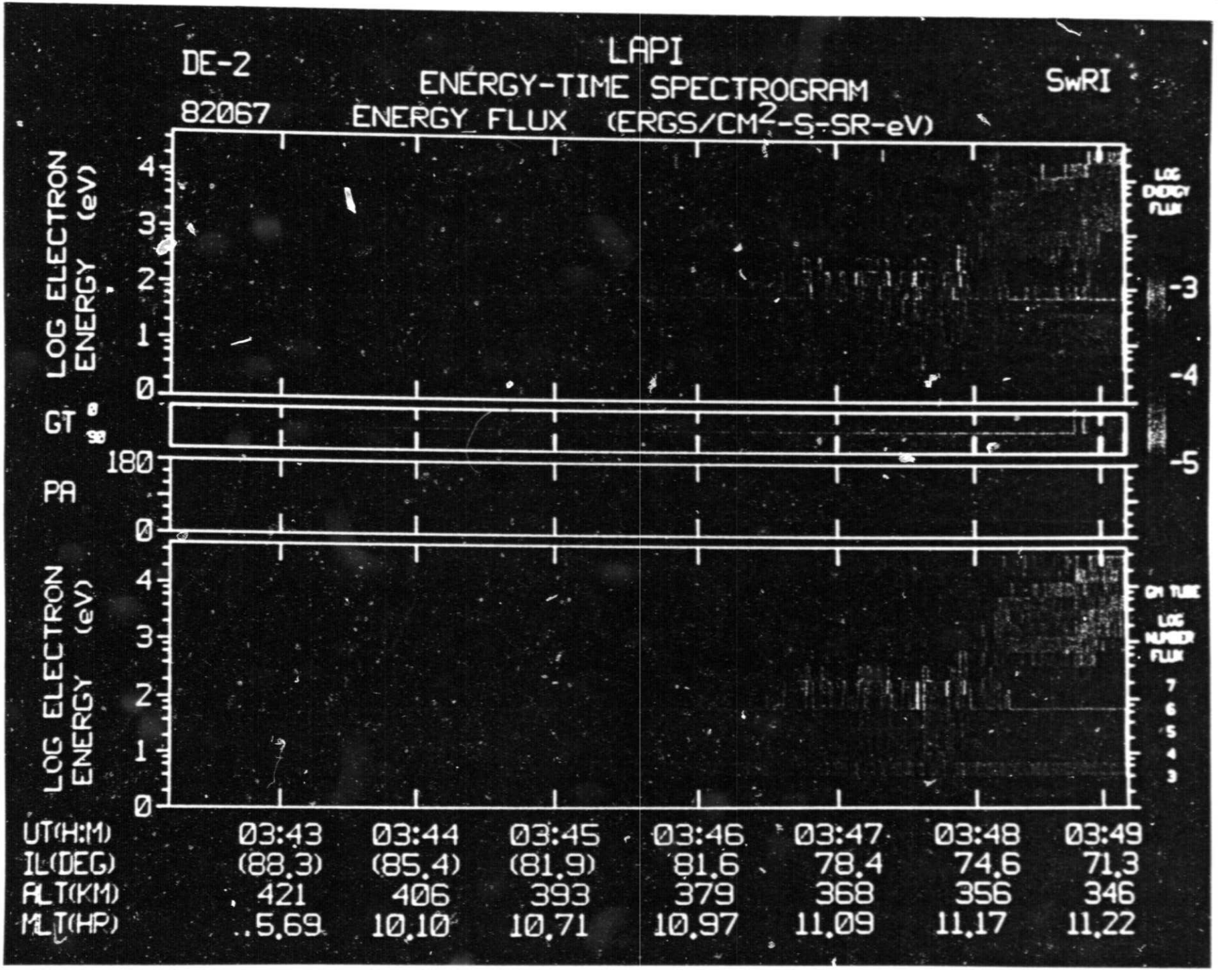

Figure 3b

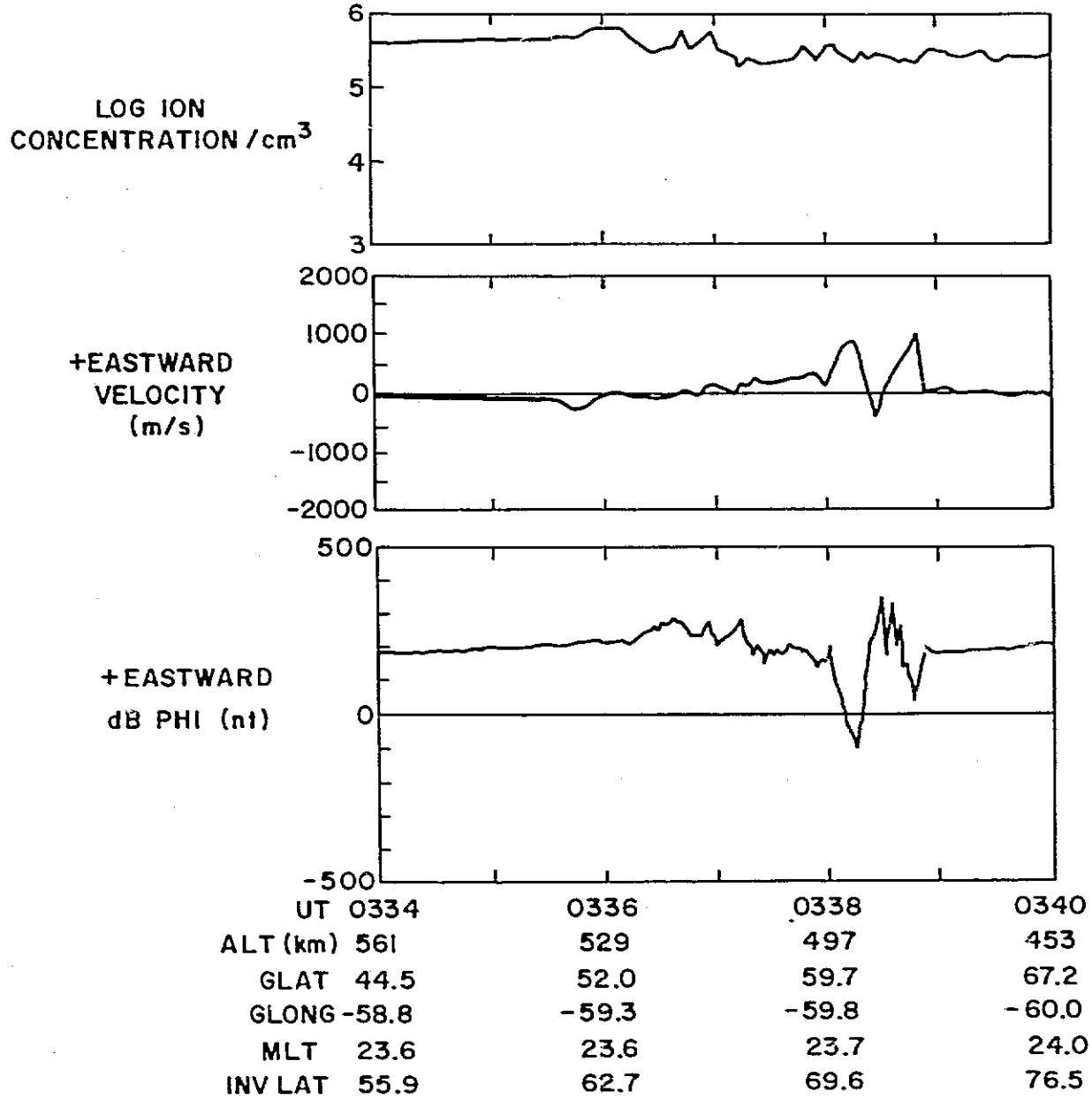
DE-2 8 MAR 1982 ORBIT #3223
LOG ION CONCENTRATION /cm3
6
5
4
3
+EASTWARD VELOCITY (m/s)
2000
1000
0
-1000
-2000
+EASTWARD dB PHI (nt)
500
0
-500
UT 0334 0336 0338 0340
ALT (km) 561 529 497 453
GLAT 44.5 52.0 59.7 67.2
GLONG -58.8 -59.3 -59.8 -60.0
MLT 23.6 23.6 23.7 24.0
INV LAT 55.9 62.7 69.6 76.5

Figure 4a

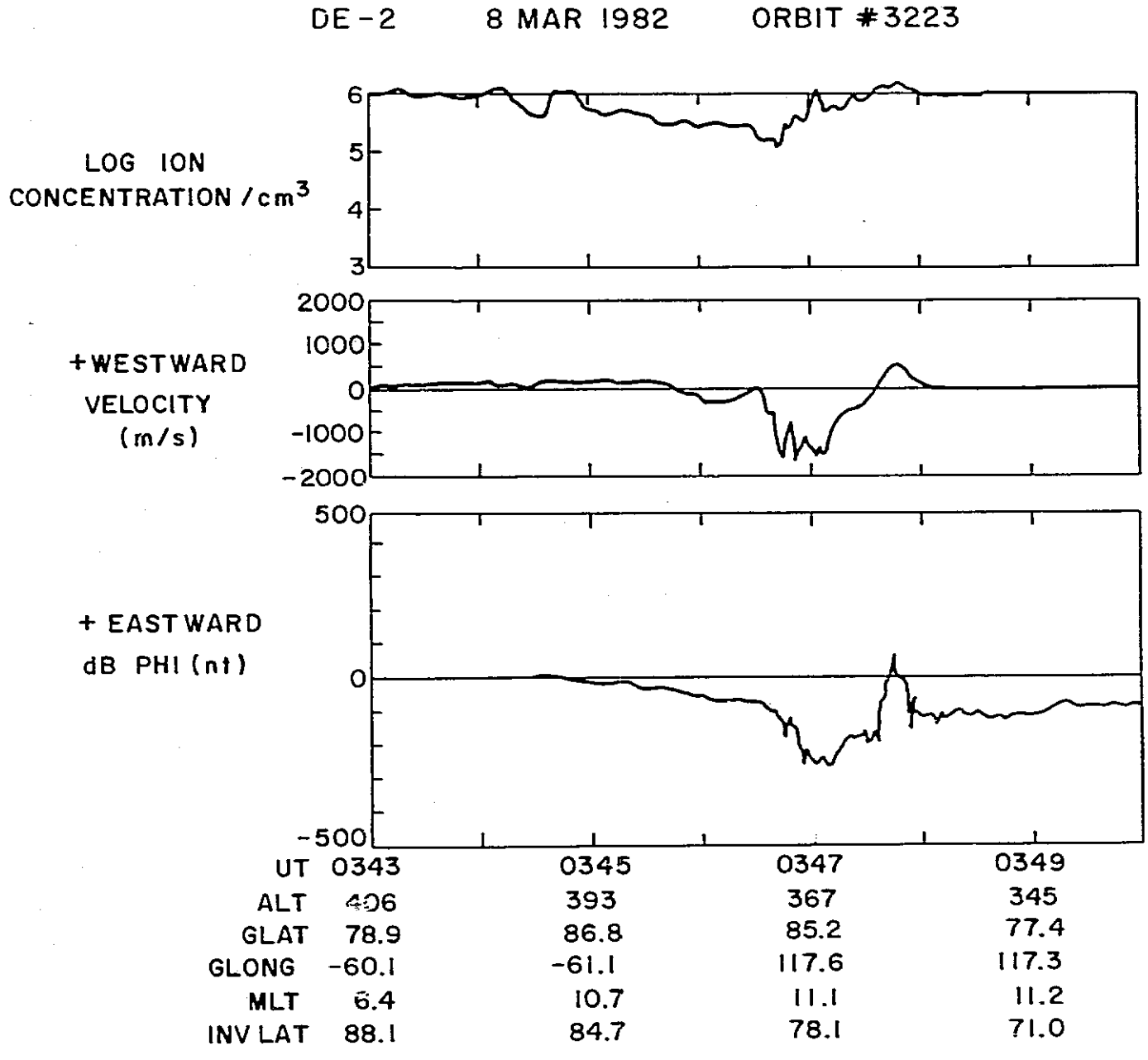
DE-2 8 MAR 1982 ORBIT #3223
LOG ION CONCENTRATION /cm3
6
5
4
3
+WESTWARD VELOCITY (m/s)
2000
1000
0
-1000
-2000
+ EASTWARD dB PHI (nt)
500
0
-500
UT 0343 0345 0347 0349
ALT 406 393 367 345
GLAT 78.9 86.8 85.2 77.4
GLONG -60.1 -61.1 117.6 117.3
MLT 6.4 10.7 11.1 11.2
INV LAT 88.1 84.7 78.1 71.0

Figure 4b

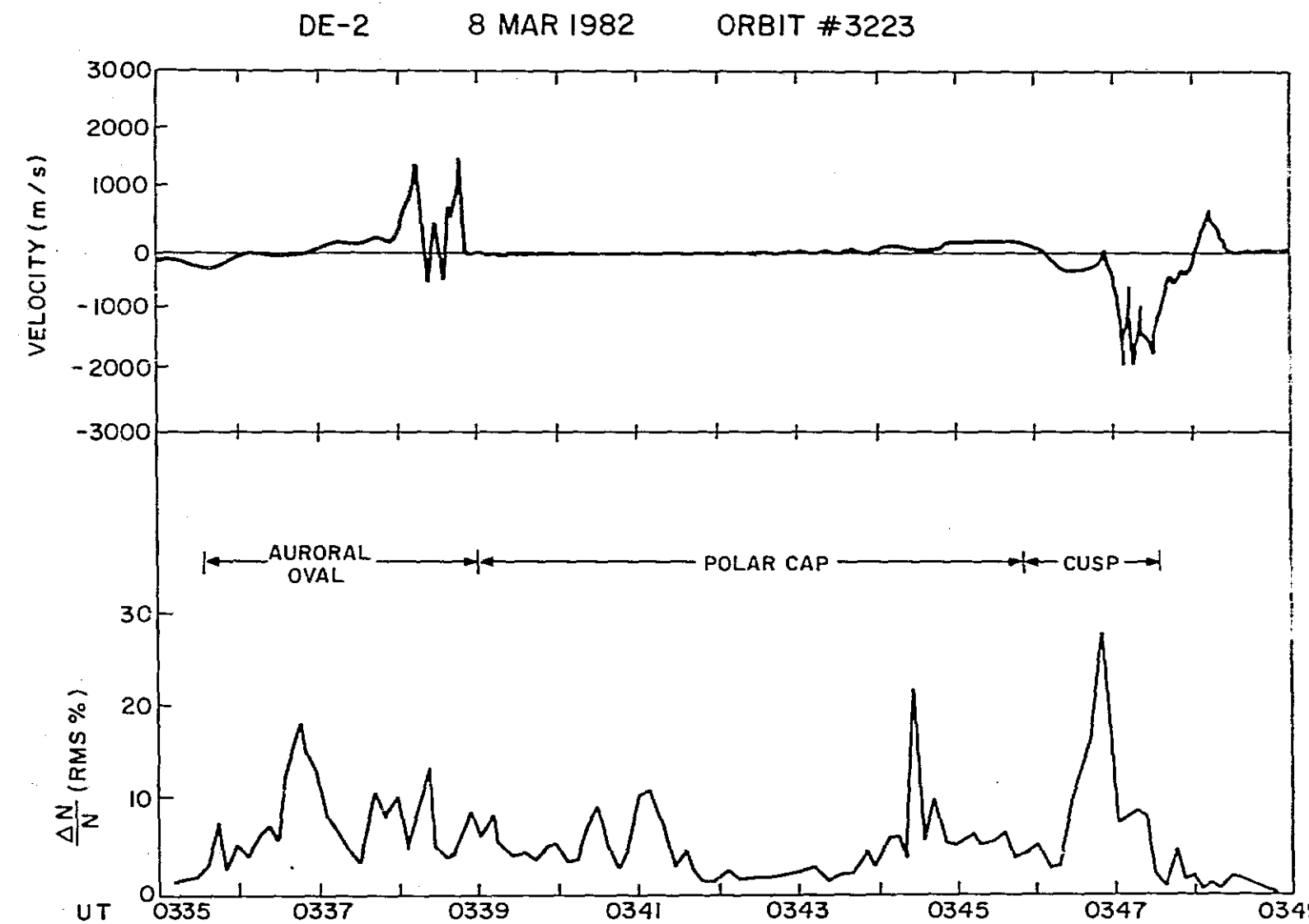
DE-2 8 MAR 1982 ORBIT #3223
VELOCITY (m/s)
3000
2000
1000
0
-1000
-2000
-3000
AURORAL OVAL
POLAR CAP
CUSP
ΔN/N (RMS %)
30
20
10
0
UT 0335 0337 0339 0341 0343 0345 0347 0349
ALT (km) 545 480 406 345
GLAT 48.3 63.5 82.9 77.3
GLONG -59.1 -60.0 -61.1 117.3
MLT 23.6 23.8 10.1 11.2
INV LAT 59.3 73.1 70.9

Figure 5

DE-2 MAR. 8, 1982 ORBIT #3223

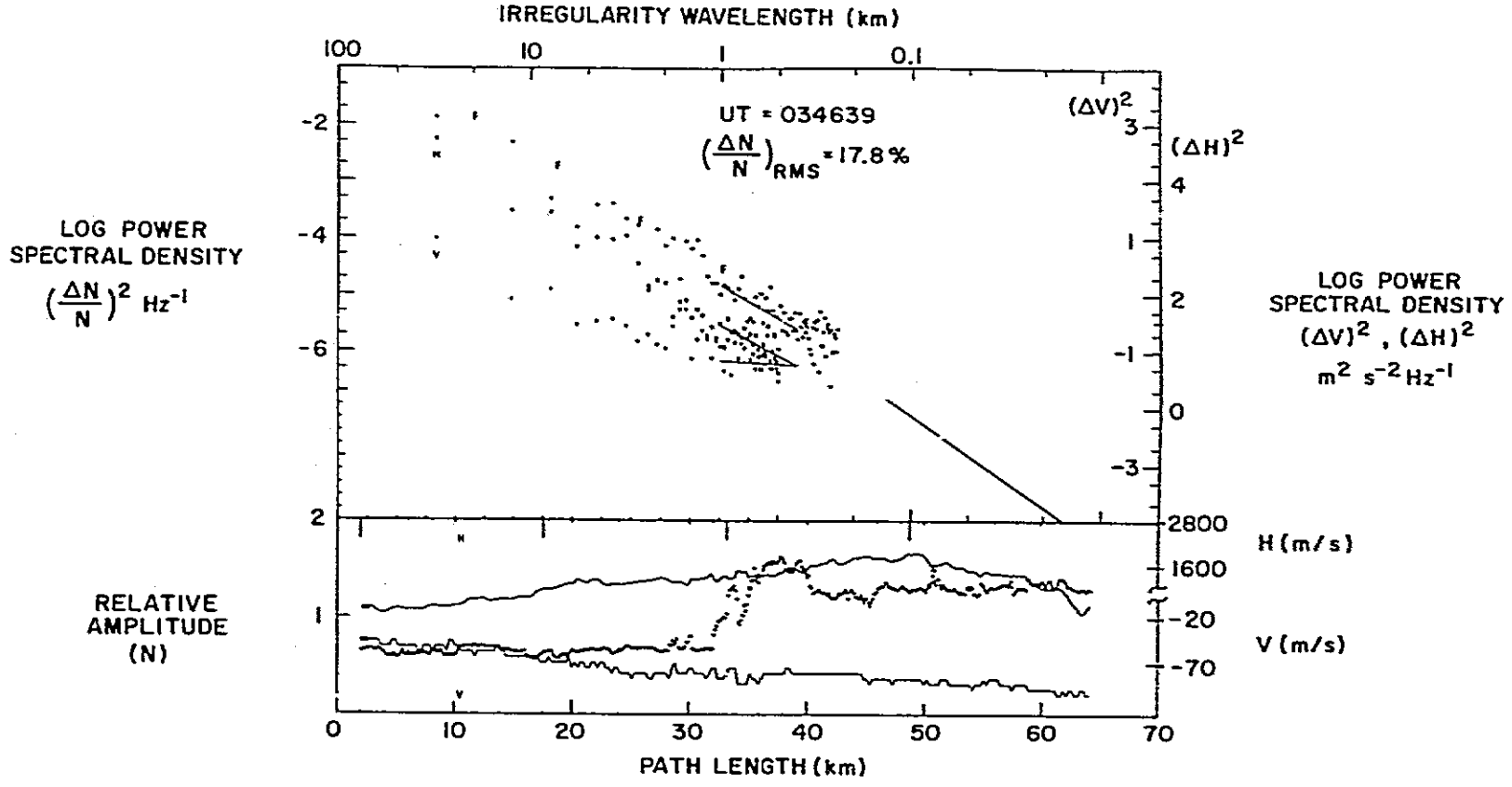

Figure 6a

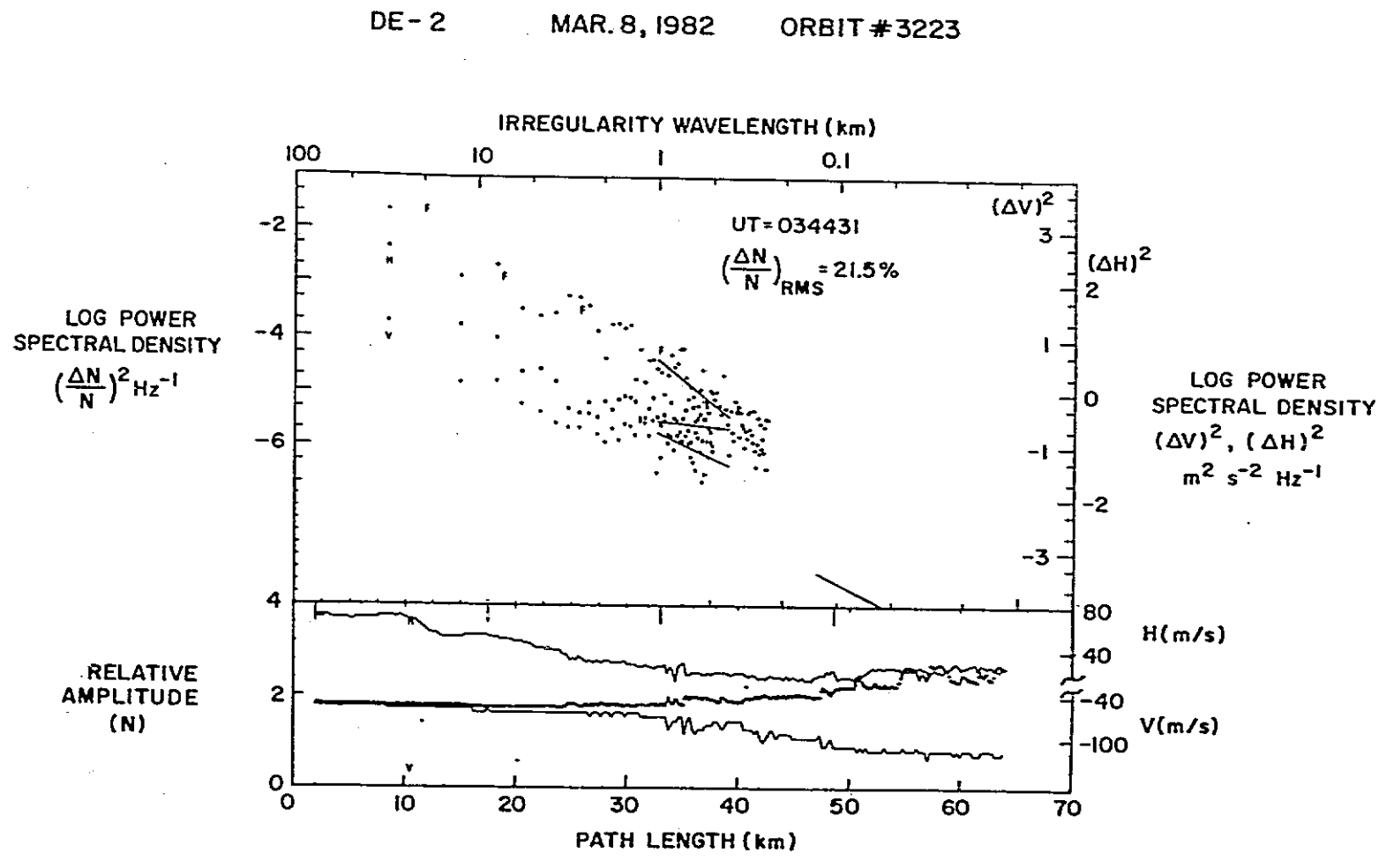
DE-2 MAR. 8, 1982 ORBIT #3223
IRREGULARITY WAVELENGTH (km)
100
10
1
0.1
UT=034431
$(\frac{\Delta N}{N})_{RMS}$ = 21.5%
LOG POWER SPECTRAL DENSITY
$(\frac{\Delta N}{N})^2 Hz^{-1}$
$(\Delta V)^2$
$(\Delta H)^2$
LOG POWER SPECTRAL DENSITY
$(\Delta V)^2$, $(\Delta H)^2$
$m^2 s^{-2} Hz^{-1}$
RELATIVE AMPLITUDE (N)
H(m/s)
V(m/s)
PATH LENGTH (km)

Figure 6b

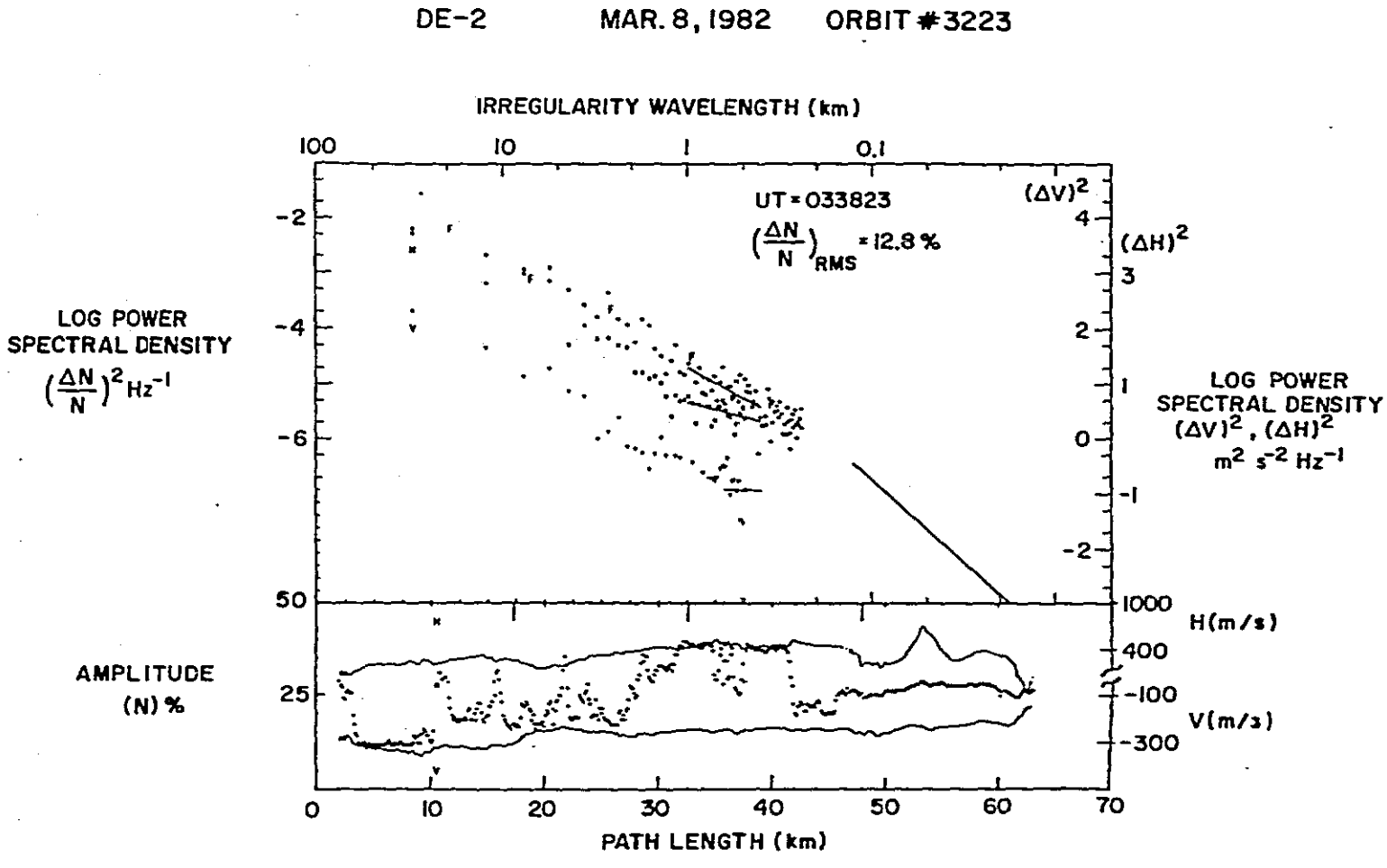
DE-2 MAR. 8, 1982 ORBIT #3223
IRREGULARITY WAVELENGTH (km)
100
10
1
0.1
UT = 033823
$\left(\frac{\Delta N}{N}\right)_{RMS}$ = 12.8 %
LOG POWER SPECTRAL DENSITY $\left(\frac{\Delta N}{N}\right)^2 Hz^{-1}$
$(\Delta V)^2$
$(\Delta H)^2$
LOG POWER SPECTRAL DENSITY $(\Delta V)^2$, $(\Delta H)^2$ $m^2 s^{-2} Hz^{-1}$
-2
-4
-6
4
3
2
1
0
-1
-2
AMPLITUDE (N) %
50
25
1000
400
-100
-300
H(m/s)
V(m/s)
0
10
20
30
40
50
60
70
PATH LENGTH (km)

Figure 6c

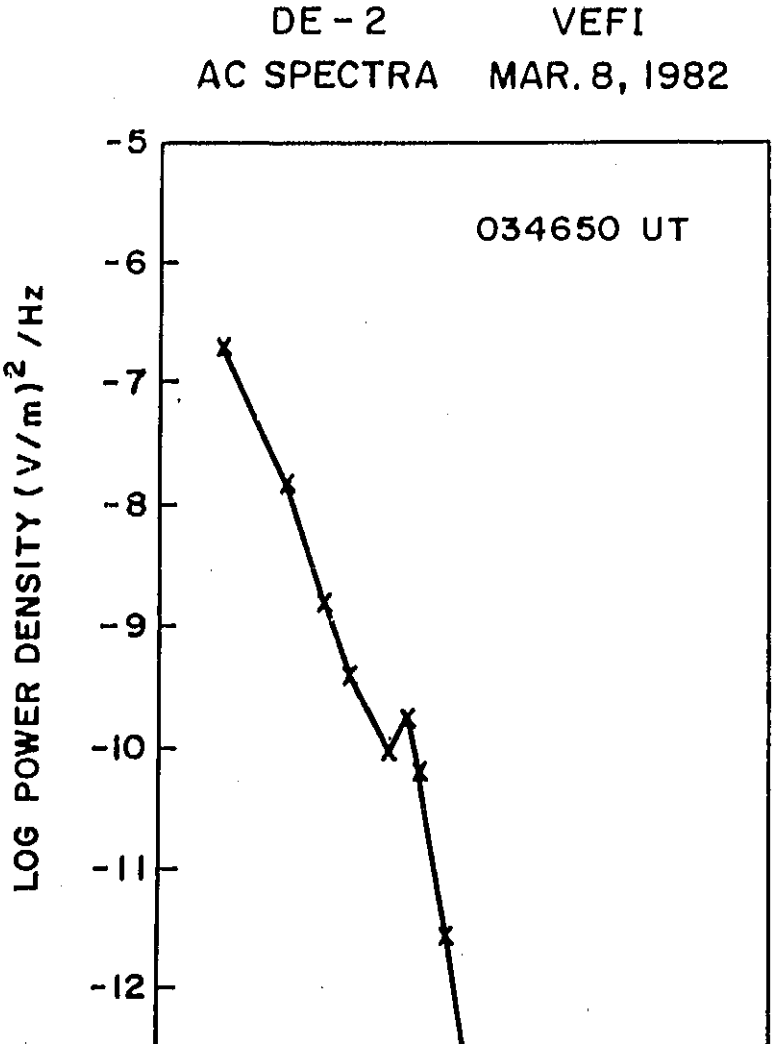
DE-2 VEFI
AC SPECTRA MAR. 8, 1982
034650 UT
LOG POWER DENSITY (V/m)² /Hz
-5
-6
-7
-8
-9
-10
-11
-12
-13
0
1
2
3
4
5
6
LOG FREQUENCY (Hz)

Figure 7a

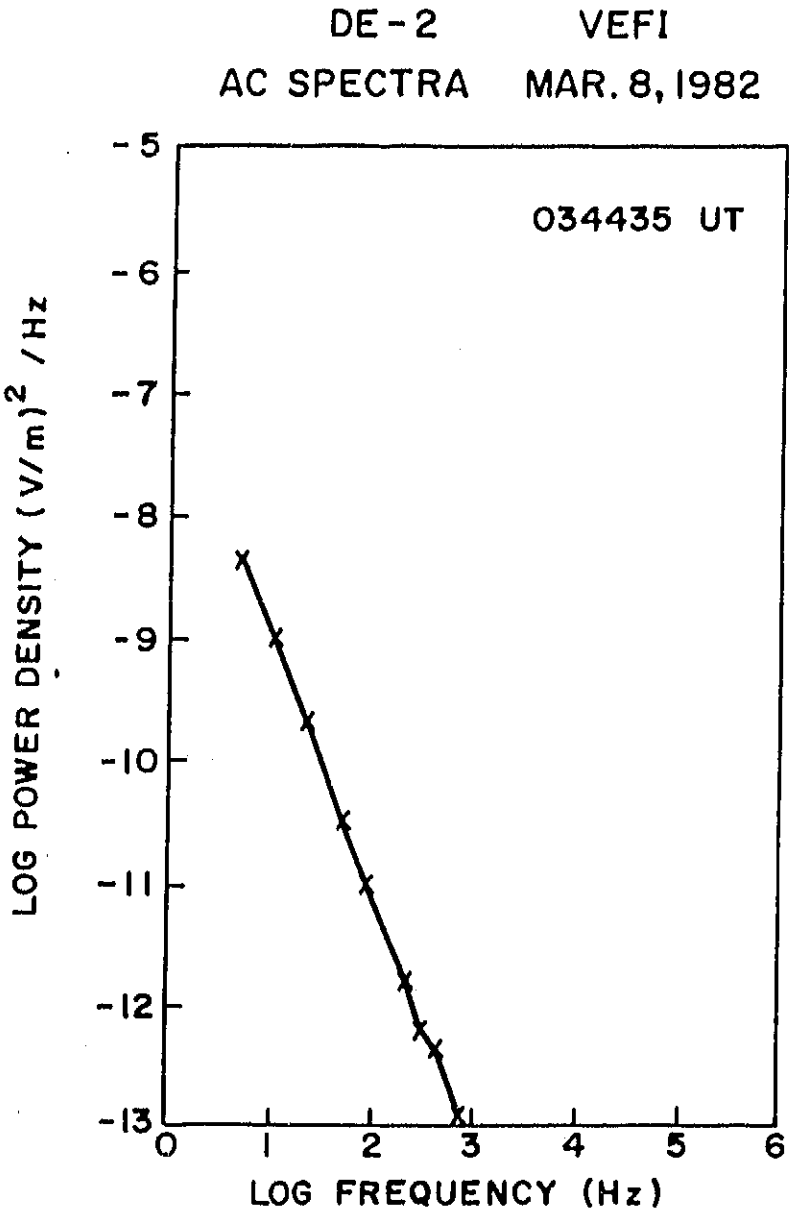
DE-2 VEFI
AC SPECTRA MAR. 8, 1982
034435 UT
LOG POWER DENSITY (V/m)^2 /Hz
-5
-6
-7
-8
-9
-10
-11
-12
-13
0
1
2
3
4
5
6
LOG FREQUENCY (Hz)

Figure 7b

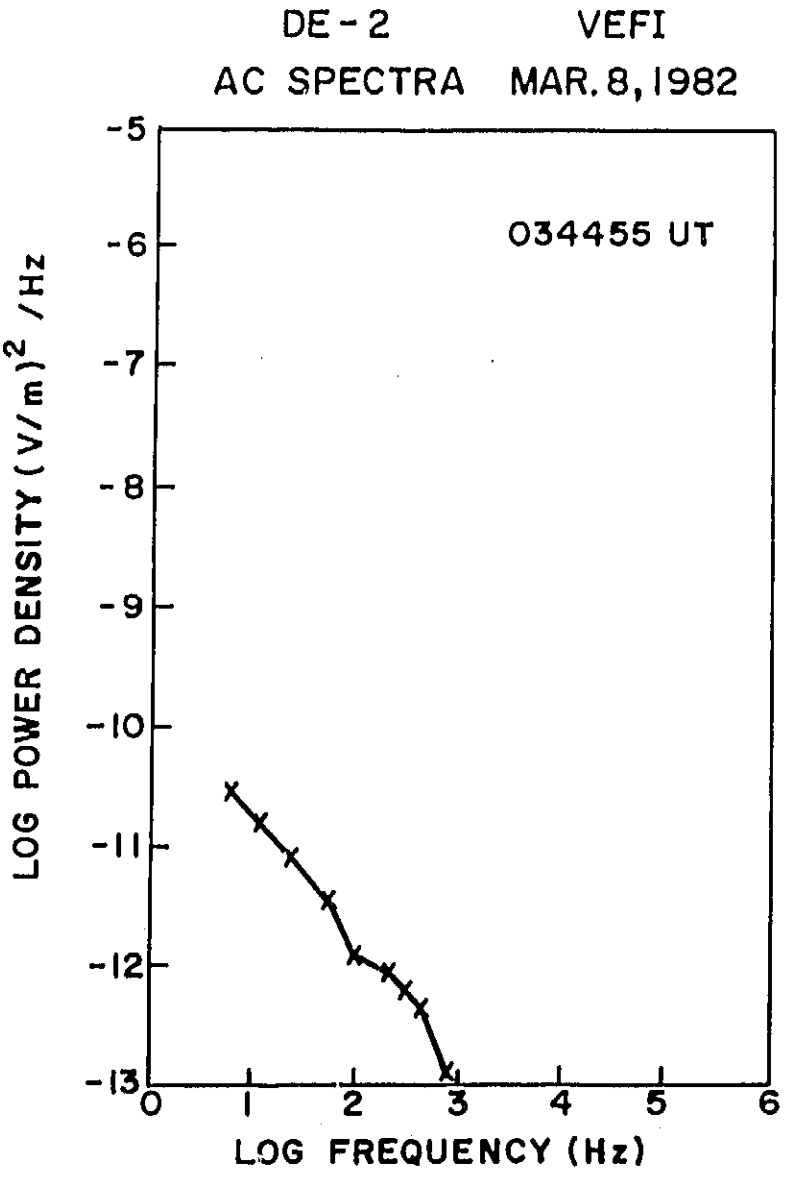
DE-2 VEFI
AC SPECTRA MAR. 8, 1982
034455 UT
LOG POWER DENSITY (V/m)^2 /Hz
-5
-6
-7
-8
-9
-10
-11
-12
-13
0
1
2
3
4
5
6
LOG FREQUENCY (Hz)

Figure 7c

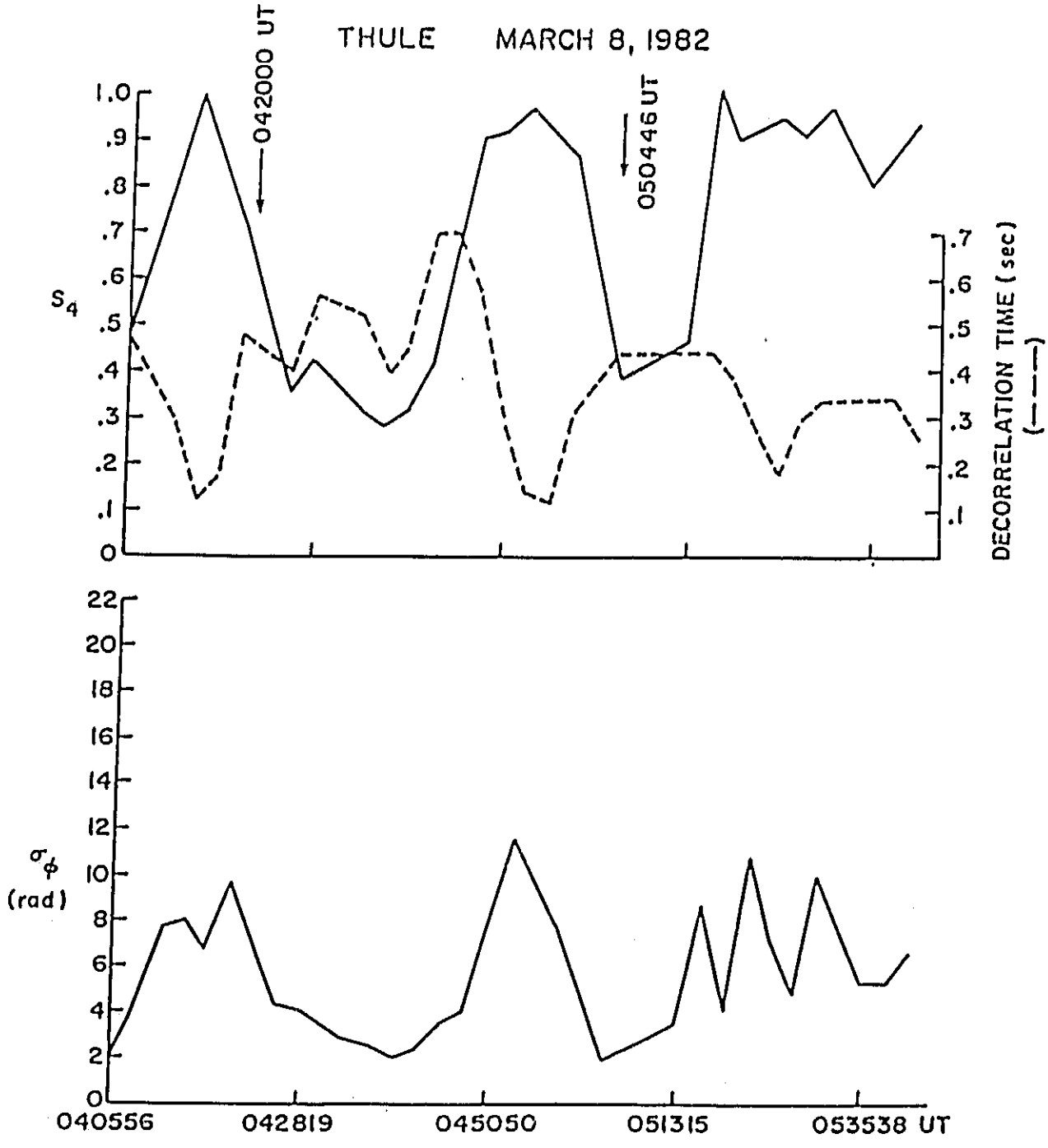
THULE MARCH 8, 1982
042000 UT
050446 UT
S_4
DECORRELATION TIME (sec)
(——)
σ_ϕ
(rad)
040556
042819
045050
051315
053538 UT

Figure 8

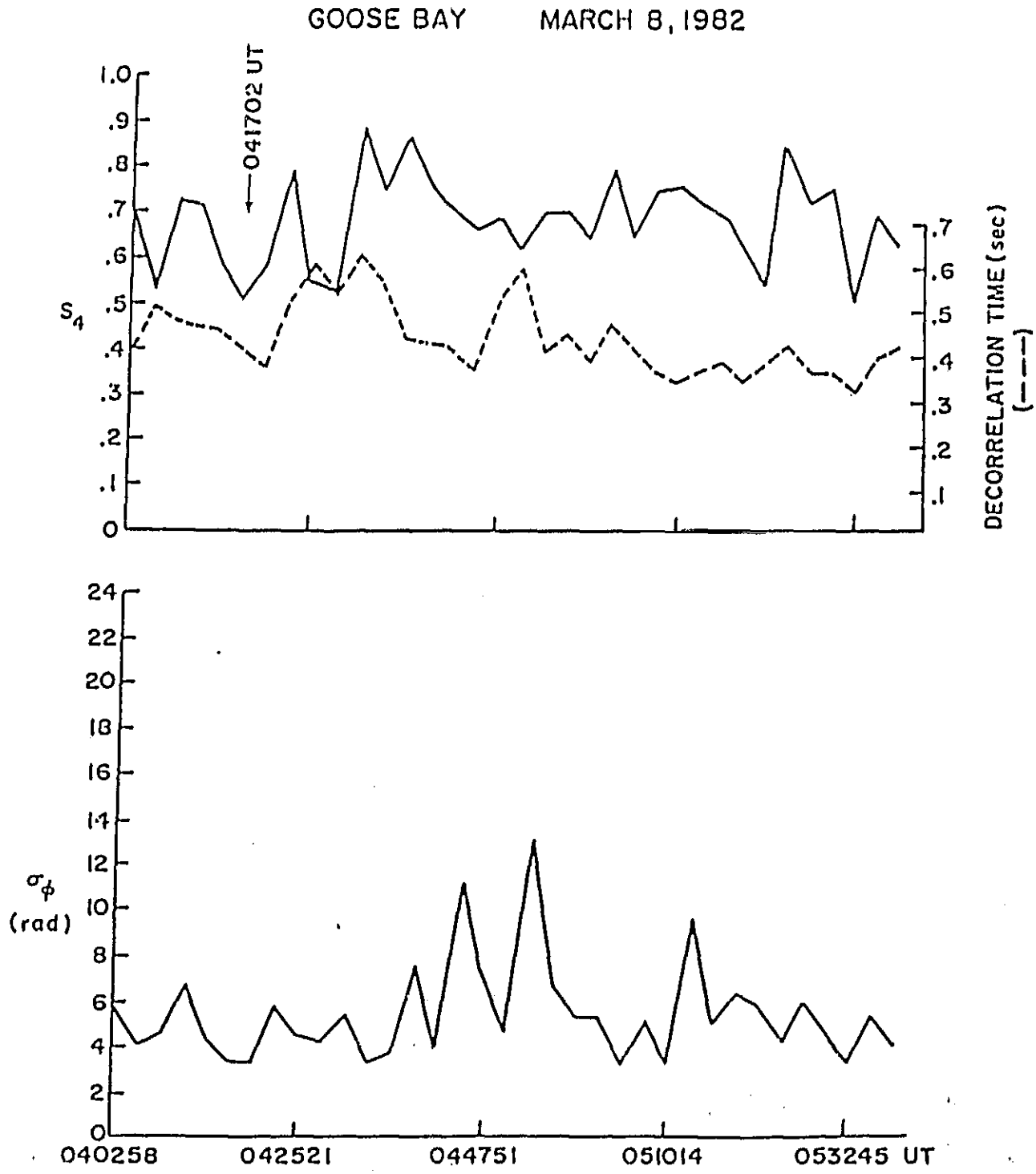
GOOSE BAY MARCH 8, 1982
041702 UT
S_4
DECORRELATION TIME (sec)
(———)
σ_ϕ
(rad)
040258
042521
044751
051014
053245 UT

Figure 9